Quantifying the controls on potential soil production rates: A case study of the San Gabriel Mountains, California

Jon D. Pelletier

Department of Geosciences, University of Arizona, Gould-Simpson Building, 1040 East Fourth Street, Tucson, Arizona 85721-0077, USA

Correspondence to: Jon D. Pelletier (jdpellet@email.arizona.edu)

Abstract. The potential soil production rate, i.e., the upper limit at which bedrock can be converted into transportable material, limits how fast erosion can occur in mountain ranges in the absence of widespread landsliding in bedrock or intact regolith. Traditionally, the potential soil production rate has been considered to be solely dependent on climate and rock characteristics. Data from the San Gabriel Mountains of California, however, suggest that topographic steepness may also influence potential soil production rates. In this paper I test the hypothesis that topographically induced stress opening of pre-existing fractures in the bedrock or intact regolith beneath hillslopes of the San Gabriel Mountains increases potential soil production rates in steep portions of the range. A mathematical model for this process predicts a relationship between potential soil production rates and average slope consistent with published data. Once the effects of average slope are accounted for, evidence that temperature limits soil production rates at the highest elevations of the range can also be detected. These results confirm that climate and rock characteristics control potential soil production rates, but that the porosity of bedrock or intact regolith can evolve with topographic steepness in a way that enhances the persistence of soil cover in compressive-stress environments. I develop an empirical equation that relates potential soil production rates in the San Gabriel Mountains to the average slope and a climatic index that accounts for temperature limitations on soil production rates at high elevations. Assuming a balance between soil production and erosion rates at the hillslope scale, I illustrate the interrelationships among potential soil production rates, soil thickness, erosion rates, and topographic steepness that result from the feedbacks among geomorphic, geophysical, and pedogenic processes in the San Gabriel Mountains.

Keywords: soil production, cosmogenic radionuclides, topographically induced stress, San Gabriel Mountains

1 Introduction

The potential soil production rate (denoted herein by P_0) is the highest rate, achieved when soil cover is thin or absent, that bedrock or intact regolith can be converted into transportable material at each point on Earth's surface. P_0 values are the rate-limiting step for erosion in areas where landsliding in bedrock or intact regolith is not widespread, because soil must be

produced before it can be eroded. Slope failure in bedrock or intact regolith is common in some fine-grained sedimentary rocks (e.g., Griffiths et al., 2004; Roering et al., 2005) but relatively uncommon in granitic rock types.

Despite its fundamental importance, the geomorphic community has no widely accepted conceptual or mathematical model for potential soil production rates. Pelletier and Rasmussen (2009) took an initial step towards developing such a model by relating P_0 values in granitic landscapes to mean annual precipitation and temperature values. The goal of this model was to quantify how water availability and vegetation cover control the potential soil production rate across the extremes of Earth's climate. The Pelletier and Rasmussen (2009) model predicts P_0 values consistent with those reported in the literature from semi-arid climates, where P_0 values typically range from ~30-300 m/Myr. In humid climates, the Pelletier and Rasmussen (2009) model predicts P_0 values greater than 1000 m/Myr (Fig. 2A of Pelletier and Rasmussen, 2009). This is broadly consistent with measured soil production rates of up to 2500 m/Myr in the Southern Alps of New Zealand where the mean annual precipitation (MAP) exceeds 10 m (Larsen et al., 2014). The Pelletier and Rasmussen (2009) model was a useful first step, but clearly not all granites are the same. In particular, variations in mineralogy (Hahm et al., 2014) and bedrock fracture density (Goodfellow et al., 2014) can result in large variations in soil production rates in granites within the same climate.

The San Gabriel Mountains (SGM) of California (Fig. 1) have been the focus of many studies of the relationships among tectonic uplift rates, climate, geology, topography, and erosion (e.g., Lifton and Chase, 1992; Spotila et al., 2002; DiBiase et al., 2010; 2012; DiBiase and Whipple, 2011; Heimsath et al., 2012; Dixon et al., 2012). These studies take advantage of a significant west-to-east gradient in exhumation rates in this range. Spotila et al. (2002) documented close associations among exhumation rates, mean annual precipitation (MAP) rates, and the locations and densities of active tectonic structures. Mean annual precipitation (MAP) rates vary by a factor of two across the elevation gradient and exhibit a strong correlation with exhumation rates (Spotila et al., 2002, their Fig. 10). Lithology, which varies substantially across the range (Fig. 1), also controls exhumation rates. Spotila et al. (2002) demonstrated that exhumation rates are lower, on average, in rocks relatively resistant to weathering (i.e., granite, gabbro, anorthosite, and intrusive rocks) compared to the less resistant schists and gneisses of the range (Spotila et al., 2002, their Fig. 9). This lithologic control on long-term erosion rates can control drainage evolution. For example, Spotila et al. (2002) concluded that the San Gabriel River has exploited the weak Pelona Schist to form a rugged

canyon between ridges capped by more resistant Cretaceous granodiorite (e.g., Mount Baden Powell). Spotila et al. (2002) concluded that landscape evolution in the SGM was controlled by a combination of tectonics, climate, and rock characteristics.

Heimsath et al. (2012) provided a millennial-time-scale perspective on the geomorphic evolution of the SGM. These authors demonstrated that soil production rates (P) and erosion rates (E) in rapidly eroding portions of the SGM greatly exceed P_0 values in slowly eroding portions of the range. Heimsath et al. (2012) concluded that high erosion rates, triggered by high tectonic uplift rates and the resulting steep topography, cause potential soil production rates to increase above any limit set by climate and bedrock characteristics. Their results challenge the traditional view that P_0 values are controlled solely by climate and rock characteristics.

Recent research, stimulated by shallow seismic refraction and drilling campaigns, has documented the importance of topographically induced stresses on the development of new fractures (and the opening of pre-existing fractures) in bedrock or intact regolith beneath hillslopes and valleys (e.g. Miller and Dunne, 1996; Martel, 2006; 2011; Slim et al., 2014; St. Clair et al., 2015). In this process, the bulk porosity of bedrock and intact regolith evolves with topographic ruggedness (i.e., topographic slope and/or curvature). In a compressive stress environment, topographically induced stresses can result in lower compressive stresses, or even tensile stresses, in rocks beneath hillslopes. As an elastic solid is compressed, surface rocks undergo outer-arc stretching where the surface is convex-outward (i.e., on hillslopes), reducing the horizontal compressive stress near the surface and eventually inducing tensile stress in areas of sufficient ruggedness. Such stresses can generate new fractures or open pre-existing fractures in the bedrock or intact regolith, allowing potential soil production rates to increase. In this paper I test whether potential soil production rates estimated using the data of Heimsath et al. (2012) are consistent with the topographically induced stress fracture opening hypothesis in the SGM. This hypothesis predicts a relationship between P_0 values and average slope that is consistent with the data of Heimsath et al. (2012). Once the effects of average slope are accounted for, I test the hypotheses that climate, lithology, and local fault density also influence P_0 values. I then use the resulting empirical model for P_0 values to map the spatial variations in potential soil production rates, soil thickness, erosion rates, and topographic steepness across the range in order to illustrate the interrelationships among these variables.

2 Data analysis and mathematical modeling

2.1 Controls on potential soil production rates in the SGM

P_0 values for the SGM can be estimated using the residuals obtained from the regression of soil production rates to soil thicknesses reported by Heimsath et al. (2012) (their Fig. 3). The exponential form of the soil production function quantifies the decrease in soil production rates with increasing soil thickness:

$$P = P_0 e^{-h/h_0},$$ (1)

where h is soil thickness and h_0 is a length scale quantifying the relative decrease in soil production rates for each unit increase in soil thickness. Heimsath et al. (2012) obtained $h_0 = 0.32$ m for locations with an average slope, S_{av}, of less than or equal to 30° and $h_0 = 0.37$ m for locations with $S_{av} > 30°$. S_{av} is defined by Heimsath et al. (2012) as the average slope over hillslopes adjacent to each sample location. P_0 values (Supplementary Table 1) can be estimated as the residuals obtained by dividing P

10 values by the exponential term in equation (1):

$$P_{0,\text{resid}} = \begin{matrix} Pe^{h/0.32 \text{ m}} & \text{if } S_{av} \leq 30° \\ Pe^{h/0.37 \text{ m}} & \text{if } S_{av} > 30°. \end{matrix}$$ (2)

where $P_{0,\text{resid}}$ denotes P_0 values estimated using the residuals of the regression. Note that equation (2) is equivalent to subtracting the logarithms of the exponential term from the logarithms of P values, since division is equivalent to subtraction under log transformation. Log transformation is appropriate in this case because P values are positive and positively skewed

15 (i.e., there are many P values in the range of 50-200 m/Myr and a smaller number of values in the range of 200-600 m/Myr that would be heavily weighted in the analysis if the data were not log-transformed). $P_{0,\text{resid}}$ values estimated from equation (2) increase, on average, with increasing S_{av} (Fig. 2A). $P_{0,\text{resid}}$ values exhibit an abrupt increase at an S_{av} of approximately 30°.

Heimsath et al. (2012) did not include data points from locations without soil cover in their regressions because these data points appear (especially for areas with $S_{av} > 30°$) to fit below the trend of equation (1). This implies that a humped

20 production function may be at work in some portions of the SGM. The mean value of P from areas with $S_{av} \leq 30°$ that lack soil cover is 183 m/Myr, i.e., slightly higher than, but within 2σ uncertainty of, the 170 ± 10 m/Myr value expected based on the exponential soil production function fit by Heimsath et al. (2012). As such, the evidence indicates that for areas with $S_{av} \leq 30°$, data from locations with and without soil cover are both consistent with an exponential soil production function. The mean value of P from areas with $S_{av} > 30°$ that lack soil cover is 207 m/Myr, i.e., significantly lower than the 370 ± 40 m/Myr

25 expected based on the exponential soil production function. This suggests that a hump may exist in the soil production function

for steep (S_{av} > 30°) slopes as they transition to a bare (no soil cover) condition. To account for this, I estimated P_0 to be equal to 1.78P (i.e., the ratio of 370 to 207) at locations with S_{av} > 30° that lack soil cover.

The SGM has horizontal compressive stresses of ~10 MPa in an approximately N-S direction at depths of less than a few hundred meters (e.g., Sbar et al., 1979; Zoback et al., 1980; Yang and Hauksson, 2013). The development of rugged topography can lead to topographically induced fracturing of bedrock and/or opening of pre-existing fractures in compressive-stress environments (e.g., Miller and Dunne, 1996; Martel, 2006; Slim et al., 2014; St. Clair et al., 2015). Given the pervasively fractured nature of bedrock in the SGM (e.g., Dibiase et al., 2015), I assume that changes in the stress state of bedrock or intact regolith beneath hillslopes leads to the opening of pre-existing fractures (i.e., an increase in the bulk porosity of bedrock or intact regolith) rather than the fracturing of intact rock. I adopt the analytic solutions of Savage and Swolfs (1986), who solved for the topographic modification of regional compressive stresses beneath ridges and valleys oriented perpendicular to the most compressive stress direction. Savage and Swolfs (1986) demonstrated that the horizontal stress (σ_{xx}) in bedrock or intact regolith becomes less compressive under ridges as the slope increases (Fig. 3). In landscapes with a maximum slope larger than 45˚ (equivalent to an average slope of approximately 27˚ or atan(0.5) in the mathematical framework of Savage and Swolfs, 1986), bedrock or intact regolith that would otherwise be in compression develops tensile stresses close to the surface beneath hillslopes (Fig. 3A). An average slope of 27˚ is close to the threshold value of 30˚ that Heimsath et al. (2012) identified as representing the transition from low to high P_0 values in the SGM. Therefore, the abrupt increase in $P_{0,resid}$ values at approximately 30˚ is consistent with a transition from compression to tension in bedrock or intact regolith beneath hillslopes of the SGM. In addition to this sign change in the horizontal stress state in the rocks beneath hillslopes of the SGM, the Savage and Swolfs (1986) model predicts a gradual decline in horizontal compressive stress as S_{av} increases between 0 and approximately 27˚ (Fig. 3B):

$$\frac{\sigma_{xx}}{N_1} = \frac{2-4S_{av}}{(2+4S_{av})(1+4S_{av})} \tag{3}$$

where N_1 is the regional maximum compressive stress and S_{av} has units of m/m in equation (3). Equation (3) is simply equation (36) of Savage and Swolfs (1986) expressed in terms of the average slope from the drainage divide to the location of maximum slope rather than the shape parameter b/a used by Savage and Swolfs (1986). Note that the tangent of the slope angle (units of

m/m) is averaged to obtain S_{av} in all cases in this paper. However, after this averaging S_{av} is reported in degrees in some cases to facilitate comparison with the results of Heimsath et al. (2012).

Figure 3 illustrates the effects of topography on tectonic stresses only. Gravitational stresses can be included in the model by superposing the analytic solutions of Savage and Swolfs (1986) (their equations (34) and (35)) with the solutions of Savage et al. (1985) for the effects of topography on gravitational stresses (their equations (39) and (40)). The result is a three-dimensional phase space of solutions corresponding to different values of the regional tectonic stress N_1, the characteristic gravitational stress $\rho g b$ (where ρ is the density of rock, g is the acceleration due to gravity, and b is the ridge height), and the Poisson ratio μ. The effects of including gravitational stresses are (1) to increase the compression at depth via the lithostatic term (at soil depths this corresponds to an addition of ~10 kPa, which is negligible compared to the regional compressive stress of ~10 MPa in the SGM), and 2) to increase the compressive stresses near the point of inflection on hillslopes (e.g., Fig. 2a of Savage et al., 1985). These modifications do not alter the first-order behavior illustrated in Figure 3 for rocks close to the surface that are not close to hollows or other points of inflection. Section 3 provides additional discussion of the assumptions and alternative approaches to modeling topographically induced stresses.

The fit of the solid curve in Figure 2A to $P_{0,resid}$ values is based on equation (3), together with an assumption that the transition from compressive to tensile stresses triggers an step increase in $P_{0,resid}$ values over a small range of S_{av} values in the vicinity of the transition from compression to tension:

$$P_{0,S} = \begin{array}{ll} P_{0,l}\left(1 - \frac{\sigma_{xx}}{N_1}\right) & \text{if } S_{av} \leq S_l \\ P_{0,h}\left(1 - \frac{\sigma_{xx}}{N_1}\right) & \text{if } S_{av} > S_h \\ \left(P_{0,l} + \left(P_{0,h} - P_{0,l}\right)\frac{S_{av}-S_l}{S_h-S_l}\right)\left(1 - \frac{\sigma_{xx}}{N_1}\right) & \text{if } S_l \leq S_{av} < S_h \end{array} \tag{4}$$

where $P_{0,S}$ denotes the model for the dependence of P_0 values on S_{av}, $P_{0,l}$ and $P_{0,h}$ are coefficients defining the low and high values of P_0, and S_l and S_h are the average slopes defining the range over which P_0 values increase from low to high values across the transition from compression to tension. $P_{0,l}$ and $P_{0,h}$ were determined to be 170 m/Myr and 500 m/Myr based on least-squares minimization to the data (data from elevations above 2300 m were excluded because of the climatic influence described below). S_l and S_h were chosen to be 30˚ and 32˚, respectively, to characterize the abrupt increase in P_0 values in the vicinity of 30˚.

In addition to the average slope control associated with the topographically induced stress fracture opening process, a climatic control on P_0 values can be identified using cluster analysis. This type of analysis involves identifying clusters in the data defined by distinctive values of the independent variables that also have different mean values of the dependent variable. The four points colored in blue in Figure 2A are the four highest elevation samples in the dataset, with elevations $\geq$ 2300 m a.s.l. The logarithms (base 10) of this cluster have a mean value of -0.40 after subtracting the logarithms of $P_{0,S}$ to account for the average slope control on $P_{0,\text{resid}}$ values, compared with a mean of 0.00 for the logarithms of the remaining data points with $S_{av} > 30°$ (also with the logarithms of $P_{0,S}$ subtracted). Assuming a significance level of 0.05, the null hypothesis that the cluster of blue points has a mean that is indistinguishable from that of the remaining points with $S_{av} > 30°$ can be rejected based on the standard t test with unequal variances ($t = 0.021$).

Figures 4A-4C illustrate the mean annual temperature (MAT), mean annual precipitation (MAP), and existing vegetation height (EVH) for the central portion of the SGM. Above elevations of approximately 1800 m a.s.l., vegetation height decreases systematically with increasing elevation (Fig. 4D). This limitation is likely to be primarily a result of temperature limitations on vegetation growth because MAP increases with elevation up to and including the highest elevations of the range. This result is consistent with the hypothesis that vegetation is a key driver of soil production. The decrease in P_0 values with elevation is likely to be gradual rather than abrupt, and indeed there is evidence of a peak in the climatic control of P_0 values. Figure 4E plots the ratio of $P_{0,\text{resid}}$ to $P_{0,S}$ as a function of elevation. The closed circles are binned averages of the data (each bin equals 100 m in elevation). The ratio of $P_{0,\text{resid}}$ to $P_{0,S}$ (equivalent to the residuals under log transformation after the effects of average slope are removed) increases, on average, and then decreases within the range of elevations between 1500 and 2600 m, broadly similar to the trend of EVH (Fig. 4D).

Local variability in P_0 estimates due to variations in soil thickness, mineralogical variations within a given lithology, spatial variations in fracture density, etc. can be minimized by averaging P_0 values (not including the four highest-elevation points because of the climatic control) from locations that have the same average slope (Fig. 2C). This process tends to average data from the same local cluster since local clusters often have average slopes that are both equal within the cluster and different from other clusters. Figure 2C demonstrates that the predictions of the topographically induced stress fracture opening hypothesis are consistent with the observed dependence of $P_{0,\text{resid}}$ values on S_{av} values.

The average slope and climatic controls on P_0 values can be combined into a single predictive equation for P_0 values:

$$P_{0,\text{pred}} = P_{0,s} C \qquad\qquad (5)$$

where $P_{0,\text{pred}}$ denotes predicted values for P_0, C is a climatic index defined as 1 for $z < 2300$ m and 0.4 (i.e., the ratio of the mean of the logarithms of the data for $z > 2300$ m to the mean of the logarithms of remaining data points with $S_{av} > 30°$) for $z > 2300$ m. A regression of $P_{0,\text{pred}}$ values to $P_{0,\text{resid}}$ values yields an R^2 of 0.50 (Fig. 2D). When data with equal S_{av} values are averaged (i.e., the filled circles in Fig. 2D), the resulting R^2 value is 0.87.

The results of this section demonstrate that average slope and climate exert controls on P_0 values in the SGM. Although I did not find additional controls that were clearly distinct from these, it is worth discussing additional controls that I tested for. The data points colored in gray in Figure 2B are from the three rock types most resistant to weathering as determined by Spotila et al. (2002): granite, anorthosite, and the Mount Lowe intrusive suite. Spotila et al. (2002) also identified gabbro as a relatively resistant rock in the SGM, but no soil production rates are available from this rock type. Figure 2B suggests that lithology might exert some control on P_0 values. Specifically, 7 samples from the more resistant lithologies sit above the least-squares fit of equation (4) to the data, while 13 (including the 7 lowest P_0 values) sit below the least-squares fit. However, the null hypothesis that the residuals of the gray cluster after the effects of average slope are removed has a mean that is indistinguishable from the residuals of the remaining points (colored black in Figure 2B) cannot be rejected ($t = 0.21$).

Many studies have proposed a relationship between fracture density and bedrock weatherability on the basis that fractures provide additional surface area for chemical weathering and pathways for physical weathering agents to penetrate into the bedrock or intact regolith (e.g., Molnar, 2004; Molnar et al., 2007; Goodfellow et al., 2014; Roy et al., 2016a,b). The difference in erosion rates between the SGM and adjacent San Bernadino Mountains, for example, has been attributed in part to differences in fracture density between these ranges (Lifton and Chase, 1992; Spotila et al., 2002). As such, it is reasonable to hypothesize that differences in P_0 values might result from spatial variations in fracture density within each range. I computed a bedrock damage index D based on the concept that P_0 values increase in bedrock that is more pervasively fractured, together with the fact that bedrock fracture densities are correlated with local fault density in the SGM (Chester et al., 2005; Savage and Brodsky, 2011). Savage and Brodsky (2011) documented that bedrock fracture density decreases as a power-law function of distance from small isolated faults, i.e. as $r^{-0.8}$ where r is the distance from the fault. Fracture densities around larger

faults and faults surrounded by secondary fault networks can be modeled as a superposition of $r^{-0.8}$ decays from all fault strands (Savage and Brodsky, 2011). Chester et al. (2005) documented similar power-law relationships between bedrock fracture density and local fault density in the SGM specifically. I define the bedrock damage index D (Fig. 5A) as the sum of the inverse distances, raised to an exponent 0.8, from the point where the D value is being computed to every pixel in the study area were

5   a fault is located:

$$D = \sum_{\mathbf{x'}} \Delta x \left(\Delta x / |\mathbf{x} - \mathbf{x'}| \right)^{0.8} \tag{6}$$

where Δx is the pixel width, $\mathbf{x}$ is the map location where bedrock damage is being computed, and $\mathbf{x'}$ is the location of each mapped pixel in SGM where a fault exists. D has units of length since it is the sum of all fault lengths in the vicinity of a point, weighted by a power function of inverse distance. Equation (6) honors the roles of both the distance to and the local density

10   of faults documented by Savage and Brodsky (2011) because longer faults and/or more mature fault zones with many secondary faults have more pixels that contribute to the summation. The fact that a relationship exists between $P_{0,resid}$ values and D (Fig. 5B, $p = 0.035$) and between D and S_{av} (Fig. 5C, $p = 0.015$) suggests that some of the control by average slope that I have attributed to the topographically induced stress fracture opening process may reflect differences in the density of pre-existing fractures related to local fault density. However, the much higher R^2 value of the relationship between $P_{0,resid}$ and $P_{0,pred}$

15   ($R^2 = 0.50$) compared to that for the relationship between $P_{0,resid}$ and D ($R^2 = 0.08$) suggests that the topographically induced stress fracture opening process is the dominant mechanism controlling P_0 values in the SGM. In addition, this process has a stronger theoretical foundation.

2.2 Relating potential soil production rates to erosion rates and topographic steepness in the SGM

20   In this section I invoke a balance between soil production and transport at the hillslope scale in order to illustrate the interrelationships among potential soil production rates, erosion rates, soil thicknesses, and average slopes across the SGM. The conceptual model explored in this section is based on the hypothesis that the average slope depends on the long-term difference between uplift and erosion rates. Uplift rates (assumed here to be equal to exhumation rates) are lower in the western portion of the SGM and higher in the eastern portion (Spotila et al., 2002, their Fig. 7b). As average slope increases in areas

25   with higher uplift rates, erosion rates increase and soils become thinner. Both of these responses represent negative feedback

mechanisms that tend to decrease the differences that would otherwise exist between uplift and erosion rates and between erosion rates and soil production rates. If the uplift rate exceeds the potential soil production rate, soil thickness becomes zero and soil production and erosion rates can no longer increase with increasing slope (in the absence of widespread landsliding in bedrock or intact regolith). In such cases, topography with cliffs or steps may form (e.g., Wahrhaftig, 1965; Strudley et al.,

5   2006; Jessup et al., 2010). However, if the potential soil production rate increases with average slope via the topographically induced stress fracture opening process, the transition to bare landscapes can be delayed or prevented as Heimsath et al. (2012) proposed. This represents an additional negative feedback or adjustment mechanism. At the highest elevations of the range, soil production is slower, most likely due to temperature limitations on vegetation growth. The interrelationship between these variables can be quantified without explicit knowledge of the uplift rate, since the relationship between soil thickness and

10   average slope implicitly accounts for the uplift rate (i.e., a smaller difference between uplift and erosion rates is characterized by a thinner soil). This conceptual model predicts positive correlations among potential soil production rates, erosion rates, and topographic steepness, and negative correlations of all of these variables with soil thickness.

Equation (5), in combination with modified versions of equations (9)&(11) of Pelletier and Rasmussen (2009), i.e.,

$$P_0 e^{-h/h_0} = E \tag{7}$$

15   and

$$\frac{\kappa S_{av}}{1-(S_{av}/S_c)^2} = EL, \tag{8}$$

predict spatial variations in erosion rates and topographic steepness associated with spatial variations in P_0 values. In equations (7)&(8), κ is a sediment transport coefficient (m^2/Myr) and L is a mean hillslope length (m). Equation (8) assumes a steady state balance between soil production and erosion, modeled via the nonlinear slope-dependent sediment flux model of Roering

20   et al. (1999) at the hillslope scale. Equation (8) assumes that the mean slope gradient at the base of hillslopes (where the sediment flux leaves the slope) of a given area can be approximated by the average slope.

Spatial variations in erosion rates can be estimated using P_0 values predicted by equation (5) if spatial variations in soil thickness can also be estimated. To do this, I developed an empirical relationship between soil thickness and slope gradient derived from the Heimsath et al. (2012) dataset (Fig. 6):

$$h = \frac{h_1}{S_{av}^b},\tag{9}$$

with best-fit coefficients of $b = 1.0$ and $h_1 = 0.06$ m ($R^2 = 0.18$, $p = 0.001$). For this regression, I shifted the soil thickness in areas with no soil upward to a small finite value (0.03 m). These areas have no soil today, but must have had some soil over geologic time scales or else no erosion would occur. Also, without some shift, the 10 data points with $h = 0$ cannot be used, biasing the analysis towards areas that have soil cover today. The 0.03 m value was chosen because this is the minimum finite soil thickness measured by Heimsath et al. (2012).

Using equation (9) as a substitution, equations (7)&(8) can be combined to obtain a single equation for topographic steepness, S_{av}:

$$\frac{S_{av}}{1-(S_{av}/S_c)^2} = \frac{L}{\kappa} P_{0,\text{pred}} \exp\left(-\frac{h_1}{h_0 S_{av}^b}\right)\tag{10}$$

Given a map of steepness obtained by solving equation (10), soil thicknesses and erosion rates can be mapped using equations (7) and (8), respectively. Note that the S_{av} value obtained by solving equation (10) is not a prediction in the usual sense, since S_{av} is an input to eqn. (10) via $P_{0,\text{pred}}$. The model can be considered to capture the effects of topographic steepness if the predicted and observed values of S_{av} have broadly similar absolute values and patterns of spatial variation.

Equations (7)&(8) are the same as equations (9)&(11) of Pelletier and Rasmussen (2009) except that their equation (9) included a term representing the bedrock-soil density contrast related to a slightly different definition of P_0 and their equation (11) assumed a depth- and slope-dependent transport relation. Here I use a slope-dependent relation because depth-dependent models depend on the average soil depth *when soil is present* (because soil must be present for transport to occur), which cannot be determined for locations where soil thickness is currently zero.

The S_{av} values predicted by equation (10) (Fig. 7C) reproduce the observed first-order patterns of topographic steepness (Fig. 7C) if $L/\kappa = 0.005$ Myr/m and $S_c = 0.8$ are used. The value $S_c = 0.8$ was chosen because it is in the middle of the range of values (i.e., 0.78-0.83) that Grieve et al. (2016) obtained for steep landscapes in California and Oregon. With this value for S_c, the best-fit value for L/κ was determined by minimizing the least-squares error between the model prediction (Fig. 7B) and observed variations in average slope (Fig. 7C). Predicted and measured S_{av} values are lowest in the Western block and higher in the Sierra Madre, Tujunga, and Baldy blocks. Soil thicknesses predicted by the model correlate inversely with slopes

and P_0 values (Fig. 7D). Erosion rates (Fig. 7E) closely follow P_0 values, but are lower in absolute value, reflecting the buffering effect of soil on bedrock physical weathering processes.

3 Discussion

The effect of topographically induced stresses on regolith production is a rapidly evolving field at the boundaries among geomorphology, geophysics, and structural geology. The results presented here, based on the Savage and Swolfs (1986) model, represents just one possible approach to the problem. Miller and Dunne (1998), for example, modified the Savage and Swolfs (1986) solutions to account for cases with vertical compressive stress gradients (their parameter *k*) larger than 1. Data from the SGM and the adjacent southwestern Mojave Desert indicate that the vertical gradient of horizontal stress in the SGM is likely less than one. Sbar et al. (1979) measured mean maximum compressive stresses at the surface equal to 16 MPa, which is similar to values measured at depths of 100-200 m obtained by Zoback et al. (1980) (their Figs. 7&10). As such, the Savage and Swolfs (1986) approach is likely to be appropriate for the SGM. In addition to the effects of variations in the depth gradient of stress, fractures can open beneath hillslopes in a direction perpendicular to the slope, parallel to the slope, or in shear. The criteria for each of these strains depends on different components and/or derivatives of the stress field. For example, Martel (2006, 2011) emphasized the vertical gradient of vertical stress, which depends on the topographic curvature instead of the slope, in driving fracturing parallel to the surface, while St. Clair et al. (2015) emphasized the ratio of the horizontal stress to the spacing between ridges and valleys. More research is needed in the SGM and elsewhere to better understand the response of bedrock and intact regolith to the 3D stress field. However, all studies agree that the extent of one or more fracture opening modes increases with topographic slope and/or curvature, often with a threshold change from compression to tension above a critical value of topographic ruggedness.

The results presented here provide a process-based understanding of the dependence of potential soil production rates on topographic steepness documented by Heimsath et al. (2012) in the SGM. These authors proposed a negative feedback in which high erosion rates trigger higher potential soil production rates, with the result that soil cover may more persistent than previously thought. The results presented here suggest that, in the SGM, the release of compressive stress in steep landscapes causes fractures beneath ridges to open, thereby allowing weathering agents to penetrate into the bedrock or intact regolith

more readily. The fact that this process requires a regional compressive stress state suggests that this it is not likely to be equally important everywhere on Earth. In cases of low regional compression or extension, the development of rugged topography in rocks with pre-existing fractures is not likely to be significant in promoting fracture opening in the rocks beneath hillslopes.

5   Heimsath et al. (2012) argued that P_0 values increase with erosion rates not just in the SGM, but globally based on the strong correlation between P and E values (their Fig. 4b). However, the results of this paper suggest that the process that leads to an increase in P_0 values with increasing topographic ruggedness in the SGM in not operative everywhere. As such, other factors might explain the global correlation between P and E values. For example, erosion rates may be limited by P_0 values (since erosion cannot occur faster than soil is produced in the absence of widespread landsliding in bedrock or intact

10   regolith). P_0 values are a function of climate, with values exceeding 1000 m/Myr in humid climates (Pelletier and Rasmussen, 2009; Larsen et al., 2014). As such, the global correlation between P and E values may, in part, be a result of water availability being important for both soil production and erosion processes. If erosion rates cannot keep pace with erosion rates, stepped topography can and does form in some cases (e.g., Wahrhaftig, 1965; Strudley et al., 2006; Jessup et al., 2010), leading to a reduction in erosion rates (as evidenced by lower soil production rates in bare areas relative to soil-covered areas (Hahm et al.,

15   2014)) despite locally steeper slopes. In such cases, P and E values are still correlated because erosion cannot occur at rates higher than P_0.

4 Conclusions

       In this paper I estimated spatial variations in the potential soil production rate, P_0, using cosmogenic-radionuclide-

20   derived soil production rates from the central San Gabriel Mountains of California published by Heimsath et al. (2012). The results demonstrate that trends in the data are consistent with the hypothesis that topographically induced stresses cause pre-existing fractures to open beneath steeper hillslopes. This model predicts an abrupt increase in P_0 values close to the average slope (approximately 30˚) where an increase is observed in the data. After the effects of topographically induced stress are accounted for, a limitation on P_0 values can be detected at the highest elevations of the range, where vegetation growth is

25   limited by temperature. There is some evidence that lithology and local fault density may also influence potential soil

production rates, but the null hypotheses that these processes are not significant cannot be ruled out with given a threshold statistical significance (false positive rate) of 0.05, or they cannot be clearly distinguished from other controls. The results of this paper demonstrate that P_0 values are solely dependent on climate and rock characteristics, but that rock characteristics evolve with topographic ruggedness in compressive stress environments. These results provide a useful foundation for additional targeted cosmogenic-radionuclide analyses in the San Gabriel Mountains and for the incorporation of methods that can further test the topographically induced stress fracture opening hypothesis such as shallow seismic refraction surveys and 3D stress modeling.

Acknowledgements

I thank Katherine Guns for drafting Fig. 1. I wish to thank Arjun Heimsath, Kelin Whipple, Simon Mudd, and four anonymous reviewers for critical reviews of earlier versions of the manuscript.

References

Chester, J.S., Chester, F.M., and Kronenberg, A.K.: Fracture surface energy of the Punchbowl fault, San Andreas system, Nature, 437, 133–136, doi:10.1038/nature03942, 2005.

Daly, C., Taylor, G.H., Gibson, W.P., Parzybok, T.W., Johnson, G.L., and Pasteris. P.: High-quality spatial climate data sets for the United States and beyond, Trans. Am. Soc. Ag. Eng., 43: 1957–1962, doi:10.13031/2013.3101, 2001.

DiBiase, R.A., Heimsath, A.M., and Whipple, K.X.: Hillslope response to tectonic forcing in threshold landscapes, Earth Surf. Process. Landf., 37, 855–865, doi:10.1002/esp.3205, 2012.

DiBiase, R.A. and Whipple, K.X.: The influence of erosion thresholds and runoff variability on the relationships among topography, climate, and erosion rate, J. Geophys. Res. Earth Surf., 116, F04036, doi:10.1029/2011JF002095, 2011.

DiBiase, R.A., Whipple, K.X., and Heimsath, A.M.: Landscape form and millennial erosion rates in the San Gabriel Mountains, CA, Earth Planet. Sci. Lett., 289(1-2), 134–144, doi:10.1016/j.epsl.2009.10.036, 2010.

DiBiase, R.A., Whipple, K.X., Lamb, M.P., and Heimsath, A.M.: The role of waterfalls and knickzones in controlling the style and pace of landscape adjustment in the western San Gabriel Mountains, California, Geol. Soc. Am. Bull., 127(3-4), 539–559, doi:10.1130/B31113.1, 2015.

Dixon, J.L., Hartshorn, A.S., Heimsath, A.M., DiBiase, R.A., and Whipple, K.X.: Chemical weathering response to tectonic forcing: A soils perspective from the San Gabriel Mountains, California, Earth Planet. Sci. Lett., 323, 40–49, doi:10.1016/j.epsl.2012.01.010, 2012.

Goodfellow, B.W., Skelton, A., Martel, S.J., Stroeven, A.P., Jansson, K.N., and Hättestrand, C.: Controls of tor formation, Cairngorm Mountains, Scotland, J. Geophys. Res. Earth Surf., 119, 225–246, doi:10.1002/2013JF002862, 2014.

Grieve, S.W.D., Mudd, S.M., Hurst, M.D., and Milodowski, D.T.: A nondimensional framework for exploring the relief structure of landscapes, Earth Surf. Dynam., 4, 309–325, doi:10.5194/esurf-4-309-2016, 2016.

Griffiths, P.G., Webb, R.H., and Melis, T.S.: Frequency and initiation of debris flows in Grand Canyon, Arizona, J. Geophys. Res., 109, F04002, doi:10.1029/2003JF000077, 2004.

Hahm W.J., Riebe, C.S., Lukens, C.E., Araki, S.: Bedrock composition regulates mountain ecosystems and landscape evolution, Proc. Nat. Acad. Sci. USA, 111, 3207–3212. doi:10.1073/pnas.1315667111, 2014.

Heimsath, A.M., DiBiase, R.A., and Whipple, K.X.: Soil production limits and the transition to bedrock dominated landscapes, Nature Geosci., 5, 210–214, doi:10.1038/ngeo1380, 2012.

Jessup, B.S., Miller, S.N., Kirchner, J.W., and Riebe, C.S.: Erosion, Weathering and Stepped Topography in the Sierra Nevada, California; Quantifying the Dynamics of Hybrid (Soil-Bedrock) Landscapes, American Geophysical Union, Fall Meeting 2010, abstract #EP41D-0736, 2010.

Koons, P.O., Upton, P., and Barker, A.D.: The influence of mechanical properties on the link between tectonic and topographic evolution, Geomorphology, 137(1), 168–180, doi:10.1016/j.geomorph.2010.11.012, 2012.

Larsen, I.J., Almond, P.C., Eger, A., Stone, J.O., Montgomery, D.R., and Malcolm, B.: Rapid soil production and weathering in the Southern Alps, New Zealand, Science, 343(6171), 637–640, doi:10.1126/science.1244908, 2014.

Lifton N.A., and Chase, C.G.: Tectonic, climatic and lithologic influences on landscape fractal dimension and hypsometry: implications for landscape evolution in the San Gabriel Mountains, California, Geomorphology, 5(1-2), 77–114, doi:10.1016/0169-555X(92)90059-W, 1992.

Martel, S.J.: Effect of topographic curvature on near-surface stresses and application to sheeting joints, Geophys. Res. Lett., 33, L01308, doi:10.1029/2005GL024710, 2006.

Martel, S.J.: Mechanics of curved surfaces, with application to surface-parallel cracks, Geophys. Res. Lett., 38, L20303, doi:10.1029/2011GL049354, 2011.

Miller, D.J., and Dunne, T.: Topographic perturbations of regional stresses and consequent bedrock fracturing, J. Geophys. Res., 101(B11), 25523–25536, doi:10.1029/96JB02531, 1996.

Molnar, P.: Interactions among topographically induced elastic stress, static fatigue, and valley incision, J. Geophys. Res., 109, F02010, doi:10.1029/2003JF000097, 2004.

Molnar, P., Anderson, R.S., and Anderson, S.P.: Tectonics, fracturing of rock, and erosion, J. Geophys. Res. Earth Surf., v. 112, F03014, doi:10.1029/2005JF000433, 2007.

Morton, D.M., and Miller, F.K.: Preliminary Geologic Map of the San Bernardino 30'x60' Quadrangle, California, v. 1.0, U.S. Geological Survey Open-File Report 03-293, Reston, Virginia, 2003.

Nourse, J.A.: Middle Miocene reconstruction of the central and eastern San Gabriel Mountains, southern California, with implications for evolution of the San Gabriel fault and Los Angeles basin, in Barth, A., ed., Contributions to the Crustal Evolution of the Southwestern United States: Boulder, Colorado, Geological Society of America Special Paper 365, 161–185, 2002.

Pelletier, J.D., and Rasmussen, C.: Quantifying the climatic and tectonic controls on hillslope steepness and erosion rate, Lithosphere, 1(2), 73–80, doi:10.1130/L3.1, 2009.

Roering, J.J., Kirchner, J.W., and Dietrich, W.E.: Evidence for nonlinear, diffusive sediment transport on hillslopes and implications for landscape morphology, Water Resour. Res., 35(3), 853–870, doi:10.1029/1998WR900090, 1999.

Roering, J.J., Kirchner, J.W., and Dietrich, W.E.: Characterizing structural and lithologic controls on deep-seated landsliding: Implications for topographic relief and landscape evolution in the Oregon Coast Range, USA, Geol. Soc. Am. Bull., 117(5/6), 654–668, doi:10.1130/B25567.1, 2005.

Roy, S.G., Koons, P.O., Upton, P., and Tucker, G.E.: Dynamic links among rock damage, erosion, and strain during orogenesis, Geology, 44(7), 583–586, doi:10.1130/G37753.1, 2016a.

Roy, S.G., Tucker, G.E., Koons, P.O., Smith, S.M., and Upton, P.: A fault runs through it: Modeling the influence of rock strength and grain-size distribution in a fault-damaged landscape, J. Geophys. Res. Earth Surf., 121, 1911–1930, doi:10.1002/2015JF003662, 2016b.

Savage, H.M., and Brodsky, E.E.: Collateral damage: Evolution with displacement of fracture distribution and secondary fault strands in fault damage zones, J. Geophys. Res., 116, B03405, doi:10.1029/2010JB007665, 2011.

Savage, W.Z., Swolfs, H.S., and Powers, P.S.: Gravitational stresses in long symmetric ridges and valleys: Int. J. Rock Mech. Min. Sci. & Geomech. Abs., 22(5), 291–302, 1985.

Savage, W.Z., and Swolfs, H.S.: Tectonic and gravitational stress in long symmetric ridges and valleys: J. Geophys. Res., v. 91, p. 3677–3685, 1986.

Sbar, M.L., Richardson, R.M., Flaccus, C., and Engelder, T.: Near-surface in situ stress: 1. Strain relaxation measurements along the San Andreas Fault in southern California, J. Geophys. Res., 89(B11), 9323–9332, doi:10.1029/JB089iB11p09323, 1984.

Spotila, J.A., House, M.A., Blythe, A.E., Niemi, N.A., and Bank, G.C.: Controls on the erosion and geomorphic evolution of the San Bernardino and San Gabriel Mountains, southern California, in Barth, A., ed., Contributions to Crustal Evolution of the Southwestern United States: Boulder, Colorado, Geological Society of America Special Paper 365, 205–230, 2002.

Strudley, M.W., Murray, A.B., and Haff, P.K.: Regolith thickness instability and the formation of tors in arid environments, J. Geophys. Res., 111, F03010, doi:10.1029/2005JF000405, 2006.

U.S. Geological Survey: LANDFIRE database, digital data available at http://www.landfire.gov/, accessed July 5, 2016.

U.S. Geological Survey and California Geological Survey: Quaternary fault and fold database for the United States, digital data available at   http//earthquakes.usgs.gov/regional/qfaults/, accessed July 5, 2016.

Wahrhaftig, C.: Stepped topography of the southern Sierra Nevada, California, Geol. Soc. Am. Bull, 76(10), 1165–1190, doi: 10.1130/0016-7606(1965)76[1165:STOTSS]2.0.CO;2, 1965.

5   Yang, W. and Hauksson, E.: The tectonic crustal stress field and style of faulting along the Pacific North America Plate boundary in Southern California, Geophys. J. Int., doi:10.1093/gji/ggt113, 2013.

Yerkes, R.F. and Campbell, R.H.: Preliminary Geologic Map of the Los Angeles 30'x60' Quadrangle, Southern California, v. 1.0, U.S. Geological Society Open-File Report 2005-1019, Reston, Virginia, 2005.

Zoback, M.D., Tsukahara, H., and Hickman, S., Stress measurements at depth in the vicinity of the San Andreas Fault:
10   Implications for the magnitude of shear stress at depth, J. Geophys. Res., 85(B11), 6157–6173, doi:10.1029/JB085iB11p06157, 1980.
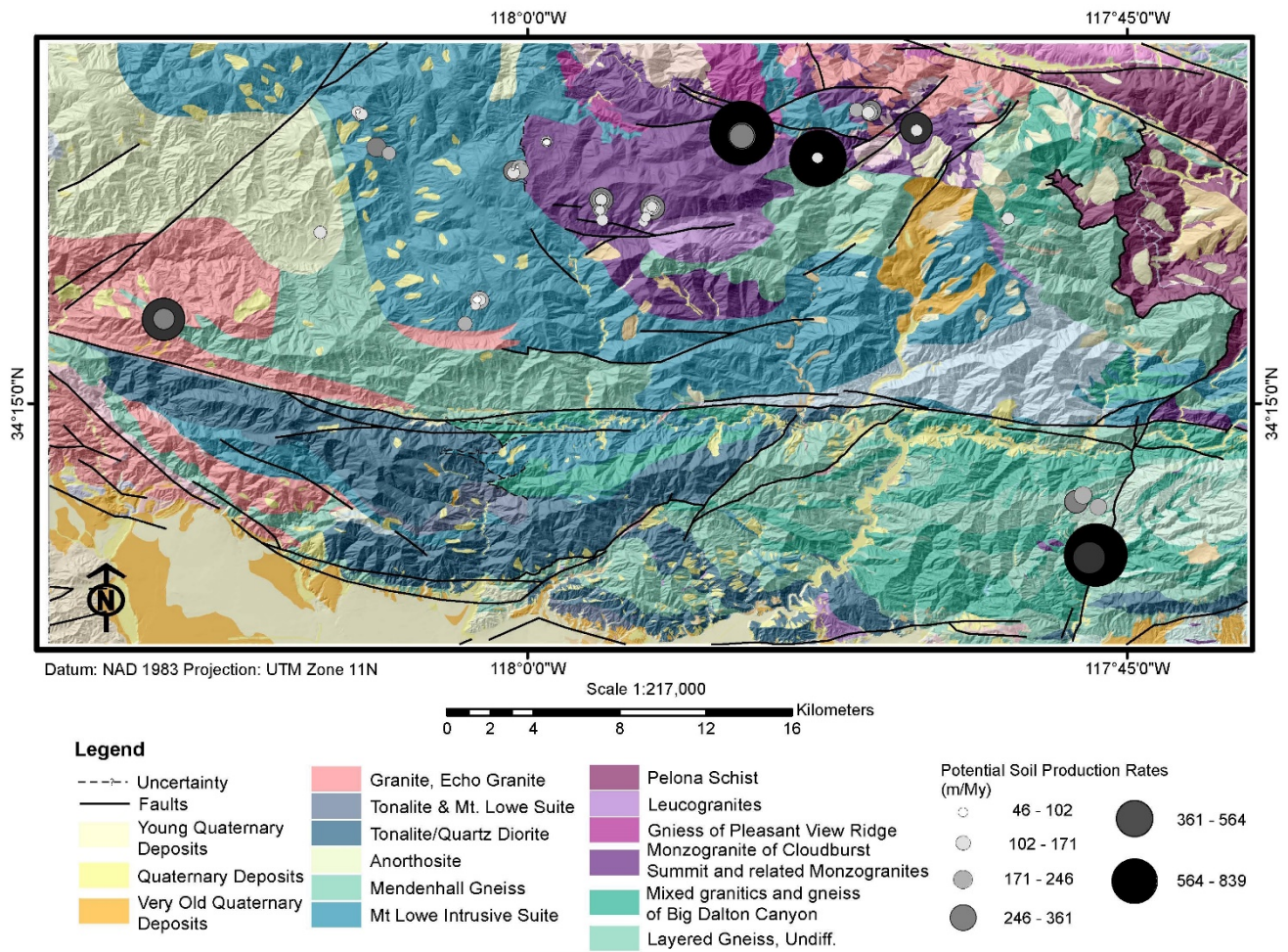
Figure 1. Geologic map of the central San Gabriel Mountains, California. Potential soil production rates inferred from the data of Heimsath et al. (2012) are also shown. Lithologic units were compiled using Yerkes and Campbell (2005), Morton and Miller (2003), and Figure 3 of Nourse (2002). Faults were mapped from Morton and Miller (2003) and the Quaternary fault and fold database of the United States (U.S. Geological Survey and California Geological Survey, 2006).
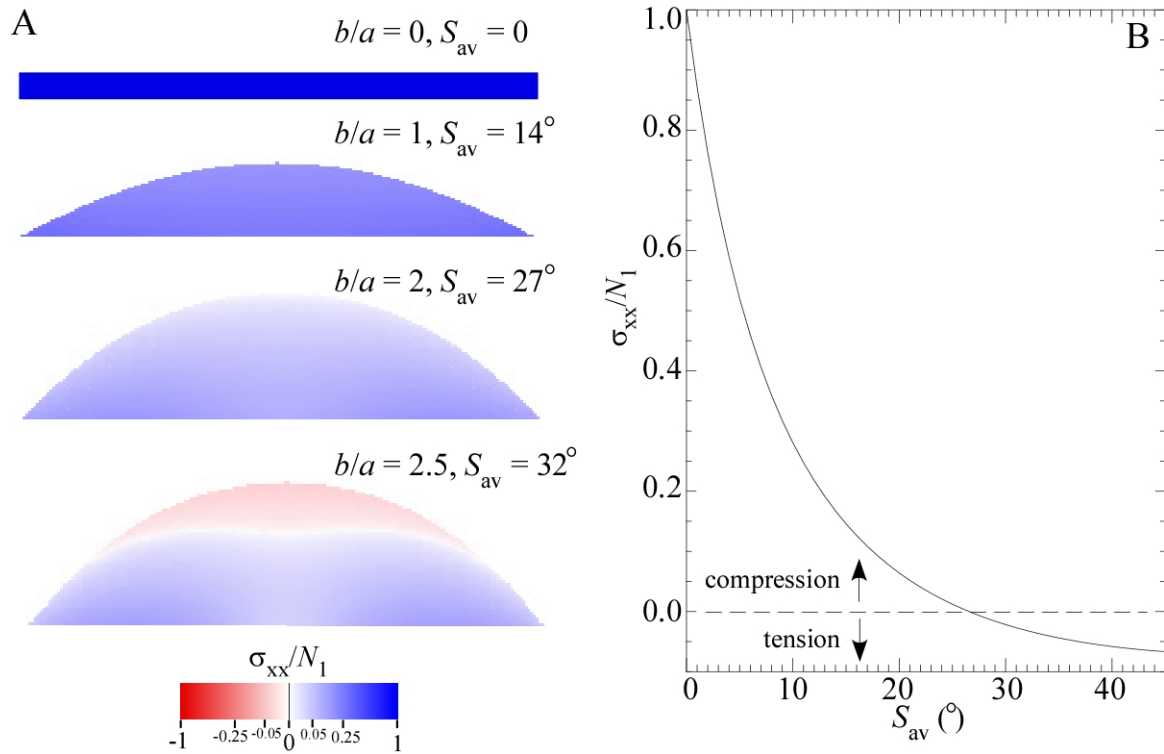
Figure 2. Analytic solutions illustrating the perturbation of a regional compressive stress field by topography. (A) Color maps of the horizontal normal stress, σ_{xx} (normalized to the regional stress, N_1), as a function of ridge steepness (defined by the shape factor b/a of Savage and Swolfs (1986) and the average slope S_{av}) using equations (34) and (35) of Savage and Swolfs (1986). The hillslopes are plotted with no vertical exaggeration. (B) Plot of σ_{xx} directly beneath the ridge as a function of S_{av} using equation (36) of Savage and Swolfs (1986). The plot illustrates the decrease in compressive stress with increasing average slope and the transition to tensile stresses at a S_{av} value of approximately 27°.

,
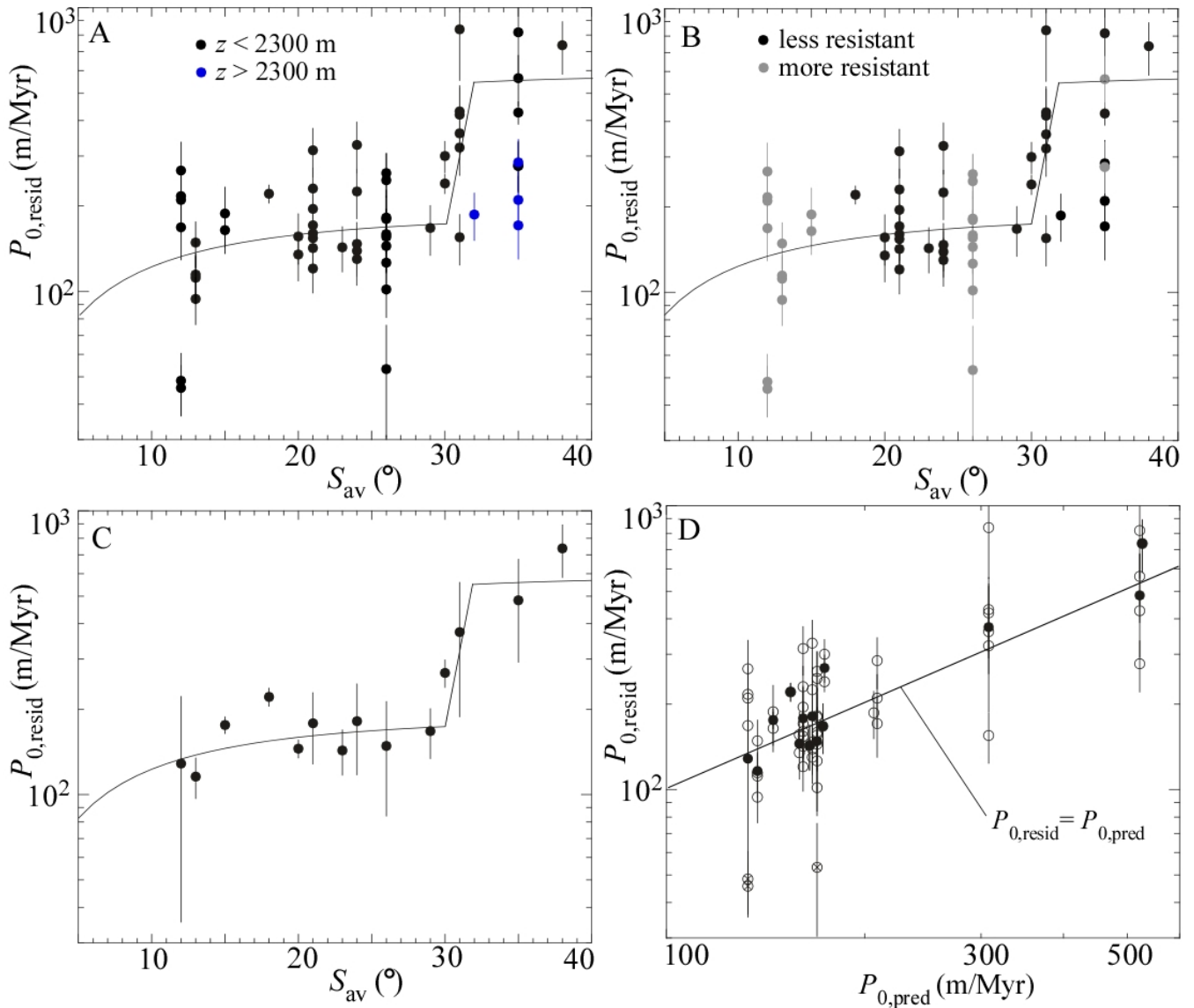
Figure 3. Plots of $P_{0,resid}$ and their relationship to average slope, S_{av}, and other potential controlling factors. (A) Plot of $P_{0,resid}$ values versus S_{av}. Data points colored blue are from the highest elevations of the range ($z > 2300$ m). **(B)** The same plot as (A), except that data points are colored according to whether they from rocks that are relatively more resistant (gray) or less resistant (black) to weathering. **(C)** Plot of $P_{0,resid}$ values averaged for each value of S_{av}. In (A) and (B), error bars represent the uncertainty of each data point, while in (C) the error bar represents the standard deviation of the data points averaged for each S_{av} value. **(D)** Plot of $P_{0,resid}$ versus values predicted from equation (5). Unfilled circles show individual data points, while filled circles represent the averaged data plotted in (C).
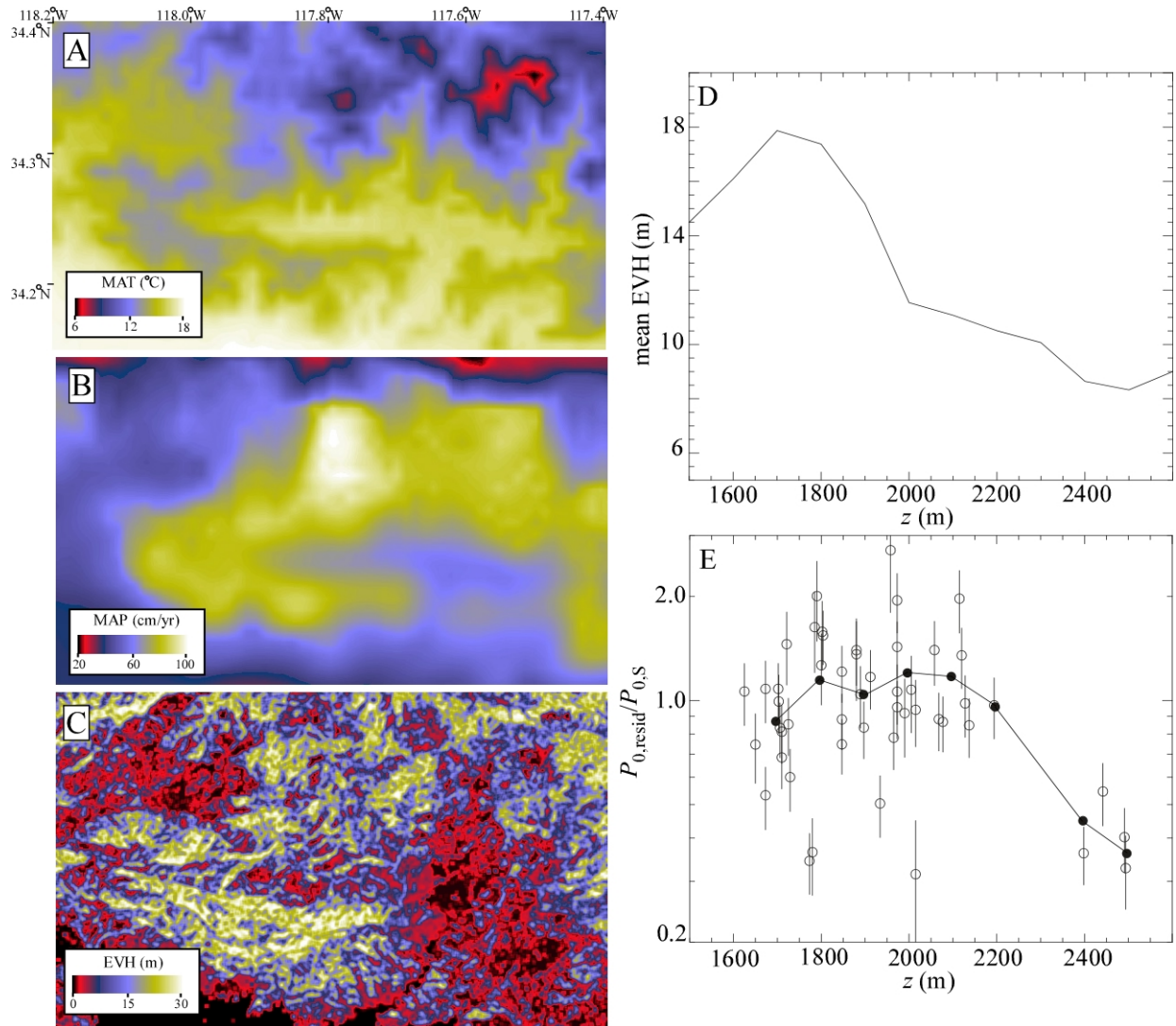
Figure 4. Climate and vegetation cover of the central San Gabriel Mountains. Color maps of (A) mean annual temperature (MAT) and (B) mean annual precipitation (MAP) from the PRISM dataset (Daly et al., 2001). (C) Color map of mean existing vegetation height (EVH) from the U.S. Geological Survey LANDFIRE database (U.S.G.S., 2016). (D) Plot of mean EVH versus elevation above sea level, z, using the data illustrated in (C). (E) Plot of the ratio of $P_{0,resid}$ to $P_{0,S}$ as a function of elevation. Filled circles are binned averages of the data (each bin equals 100 m in elevation).
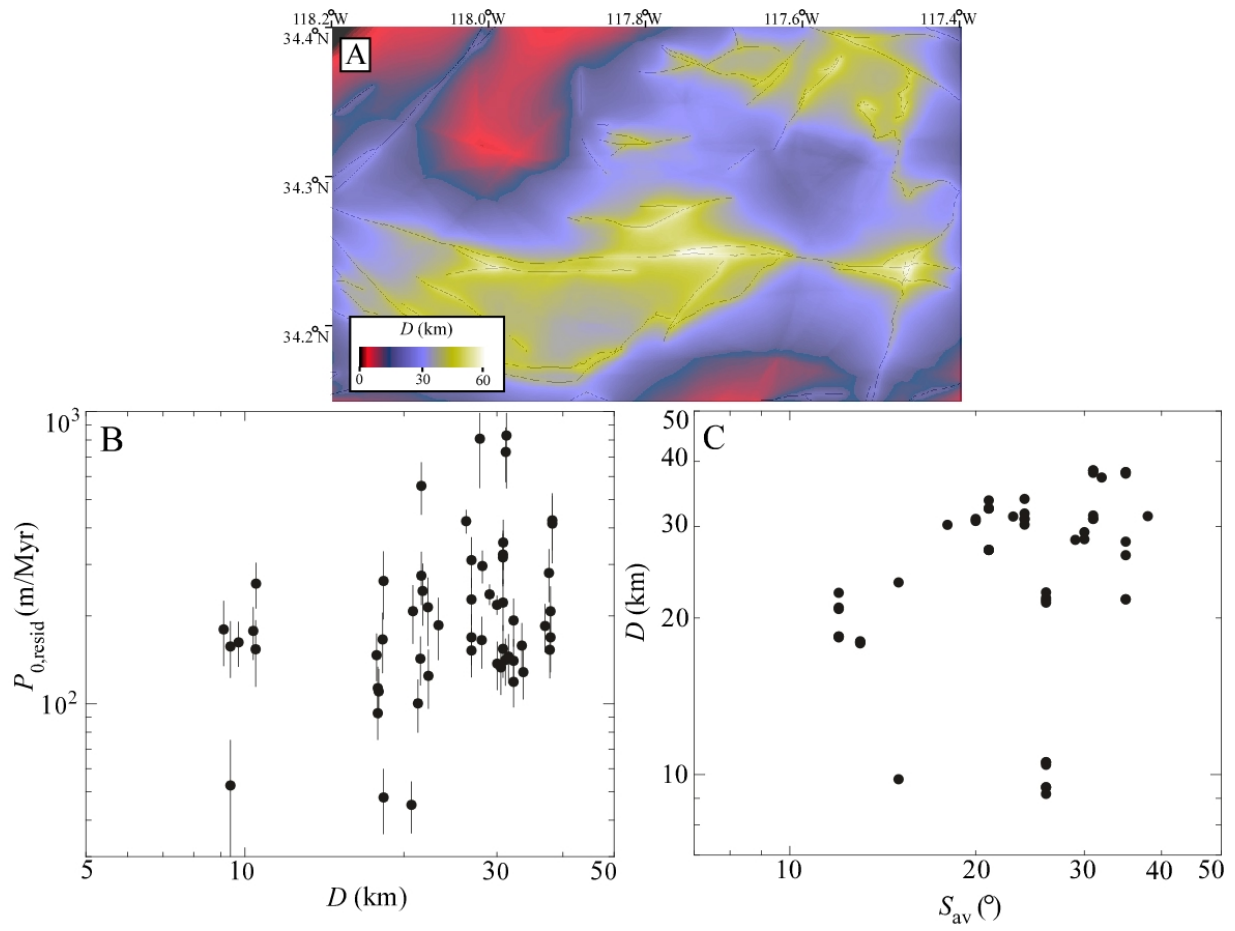
Figure 5. Map of the bedrock damage index, D, and its correlation with S_{av}. **(A)** Color map of spatial variations D. **(B)** Plot of D versus S_{av} for the 57 sample locations of Heimsath et al. (2012).
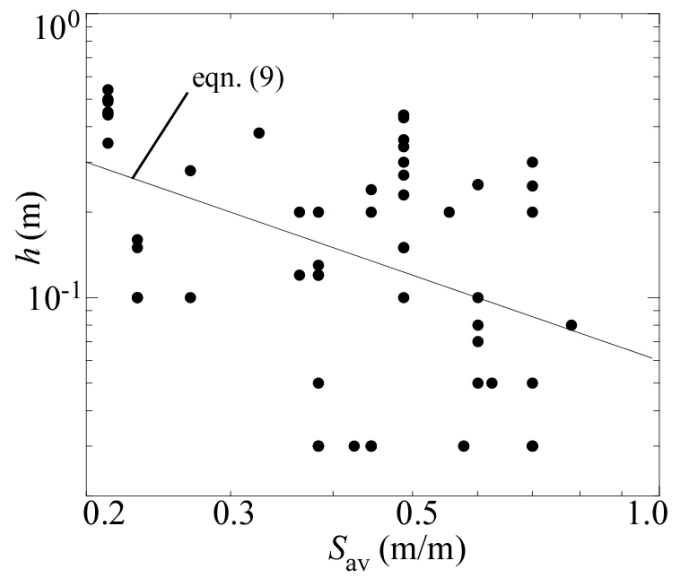
Figure 6. Plot of soil thickness, *h*, as a function of average slope, S_{av}. The least-squares power-law fit to the data (equation (9)) is also shown.
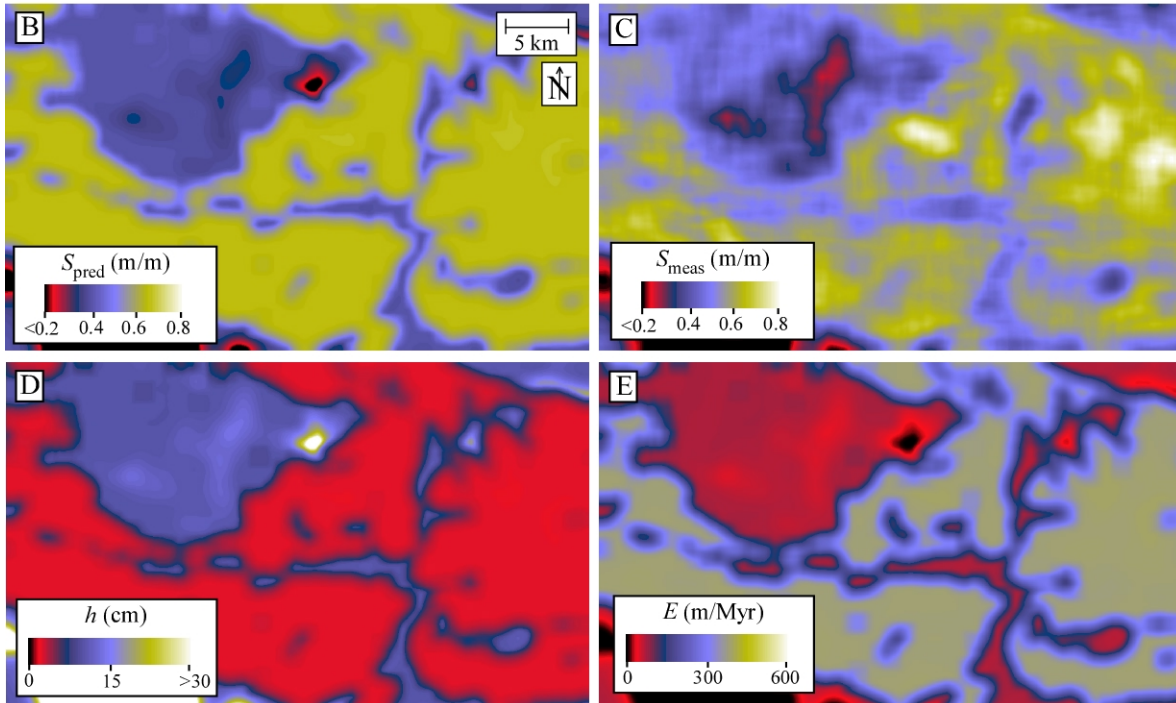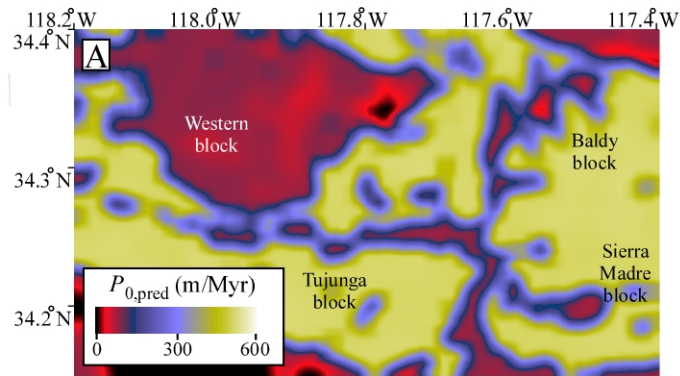
Figure 7. Color maps illustrating the predicted potential soil production rate from equation (5) ($P_{0,pred}$), predicted and observed values of average slope, S_{av}, soil thickness, h, and erosion rate, E. (A) Color map of $P_{0,pred}$ values estimated from equation (5). (B) Color map of S_{av} values predicted by equation (10), smoothed by a moving average filter with a 1-km length scale to emphasize patterns at the landscape scale. (C) Color map of actual (DEM-derived) S_{av} values, smoothed in the same manner as (B). (D) Color map of soil thicknesses, h, predicted by equation (9). (E) Color map of erosion rates, E predicted by equation (7).